

In Situ Design of High-Performance Dual-Phase GeSe Thermoelectrics by Tailoring Chemical Bonds

Lipeng Hu, Bingcai Duan, Tu Lyu,* Nan Lin, Chaohua Zhang, Fusheng Liu,* Junqin Li, Matthias Wuttig, and Yuan Yu*

Composite engineering favors high thermoelectric performance by tuning the carrier and phonon transport. Herein, orthorhombic and rhombohedral dual-phase GeSe are designed in situ by tailoring chemical bonds. Atom probe tomography verifies the coexistence of a covalently bonded orthorhombic phase and a metavalently bonded rhombohedral phase in GeSe-InTe alloys. The production of the rhombohedral phase simultaneously increases the carrier concentration, the carrier mobility, the band degeneracy, and the density-of-states effective mass due to the reduced formation energy of cation vacancies and the improved crystal symmetry. These attributes are beneficial to a high-power factor. In addition, the thermal conductivity can be significantly reduced due to the intrinsically strong lattice anharmonicity of the metavalently bonded phase, the interfacial acoustic phonon mismatch across different bonding mechanisms, and the phonon scattering at vacancy-solute clusters. Moreover, the metavalently bonded phase embraces higher solubility of dopants that enables the further optimization of properties by Cd-Ag doping, resulting in a zT of 0.95 at 773 K as well as enhanced strength and ductility in dual-phase $\text{Ge}_{0.94}\text{Cd}_{0.03}\text{Ag}_{0.03}\text{Se}(\text{InTe})_{0.15}$. This work indicates that in situ design of dual-phase composites by tailoring chemical bonds is an effective method for enhancing the thermoelectric and mechanical properties of GeSe and other p -bonded chalcogenides.

1. Introduction

Composite engineering remains the frontier topic in the field of materials science and engineering and has been employed extensively to tailor the mechanical, physical, chemical, electrochemical, and biological properties of materials.^[1] For instance, metastable high-entropy dual-phase alloys led to a combined increase in strength and ductility.^[2] In thermoelectrics, an eco-friendly energy conversion technology that can directly convert waste heat into electricity,^[3] the composite engineering affects the overall thermoelectric (TE) parameters and thus the materials' dimensionless figure of merit $zT = \alpha^2 \sigma T / (\kappa_L + \kappa_e)$, where α is the Seebeck coefficient, σ is the electrical conductivity, T is the absolute temperature, κ_L is the lattice thermal conductivity and κ_e is the electronic thermal conductivity.^[4]

According to the effective medium theory, the resulting properties of the composite material are averages, which

depend on the relative fractions of the individual components.^[5] In this vein, the TE properties of the second phase should be as high as possible. It was believed that the effective zT value of a two-component composite can never be greater than the largest value of its components.^[6] However, this conclusion overlooks the interfacial effects that provide extra degrees of freedom to tune the transport of electrons and phonons.^[7] The most intuitive and prominent effect of interfaces is to lower the lattice thermal conductivity by strong phonon scattering at interfaces. This effect has been extensively utilized in nanostructured composites.^[8] Yet, these interfaces could also scatter electrons thus causing a potential trade-off between electrical and thermal transport properties.^[9] The structural and chemical features of the interface are thus of paramount importance. Given the above scenario, we deduce that an enhancement of zT by composite engineering will be facilitated by satisfying these conditions: i) the second phase provides high TE performance that can compensate for the inferior performance of the matrix; ii) the interfaces should be coherent that can scatter phonons while having little effects on the carrier mobility μ_H . However, it is a non-trivial task to experimentally realize these requirements. Traditional composite engineering is based on the mechanical mixture of multiple components, which are subsequently solidified by sintering, where the second phase often


L. Hu, B. Duan, T. Lyu, C. Zhang, F. Liu, J. Li
College of Materials Science and Engineering
Shenzhen Key Laboratory of Special Functional Materials
Guangdong Research Center for Interfacial Engineering of Functional Materials

Guangdong Provincial Key Laboratory of Deep Earth Sciences and Geothermal Energy Exploitation and Utilization
Institute of Deep Earth Sciences and Green Energy
Shenzhen University
Shenzhen 518060, China

E-mail: tulyu@szu.edu.cn; fsliu@szu.edu.cn

N. Lin, M. Wuttig, Y. Yu
Institute of Physics (IA)
RWTH Aachen University
Sommerfeldstraße 14, 52074 Aachen, Germany
E-mail: yu@physik.rwth-aachen.de

M. Wuttig
PGI 10 (Green IT)
Forschungszentrum Jülich GmbH
52428 Jülich, Germany

 The ORCID identification number(s) for the author(s) of this article can be found under <https://doi.org/10.1002/adfm.202214854>.

© 2023 The Authors. Advanced Functional Materials published by Wiley-VCH GmbH. This is an open access article under the terms of the Creative Commons Attribution License, which permits use, distribution and reproduction in any medium, provided the original work is properly cited.

DOI: 10.1002/adfm.202214854

shows poor TE performance and mainly generates arbitrary new interfaces.^[10]

Many IV-VI chalcogenide compounds embrace different phases, providing a new opportunity to create composite materials without introducing exotic material combinations.^[11] A major problem with this strategy is that the phase transition normally occurs at high temperatures^[12] or high pressures.^[13] Recent findings demonstrate that these phase transitions are closely linked to chemical bonding mechanisms.^[14] To be more specific, the orthorhombic phase of IV-VI compounds utilizes covalent bonding, while their rhombohedral version employs metavalent bonding (MVB).^[15] MVB is a fundamental chemical bonding mechanism such as covalent, ionic, and metallic bonding but distinctively differs from them.^[14a,16] Instead of electron pairs between adjacent atoms to form a covalent bond described by Lewis,^[17] MVB is characterized by the formation of a half-filled σ -bond between p -orbital electrons. Thus, MVB compounds show a cubic or slightly distorted cubic (rhombohedral) structure with octahedral coordination. The MVB mechanism can be destroyed by increasing the degree of lattice distortion, which is generally described in the term of Peierls distortion.^[18] Phase separation is generally enabled by crossing the border between MVB and

other bonding systems such as GeTe-GeSe, where the former utilizes MVB and the latter employs covalent bonding.^[16c] Hence, tailoring chemical bonds is feasible to generate composite phases in situ with the same constituent elements in IV-VI compounds. In the meantime, since the orthorhombic, rhombohedral, and cubic phases of a compound are interconverted by the lattice distortion,^[18] the consequent slight structure difference is conducive to forming coherent interfaces.

In this work, as exemplified for GeSe-based alloys, we realized the formation of dual-phase composites with the same major constituent elements, i.e., Ge and Se, for both the rhombohedral and orthorhombic phases via tailoring the chemical bonding mechanisms. The study of GeSe thermoelectrics is of both scientific and practical significance. It could reveal the mechanisms underpinning the poor TE properties of GeSe compared with other IV-VI counterparts such as PbTe and GeTe. It also provides an earth-abundant and less-toxic alternative to them. As schematically summarized in **Figure 1**, alloying GeSe with InTe can tune the orbital overlap and thus the chemical bonding mechanisms, inducing a bonding transition from covalent to metavalent accompanied by a structural transition from the orthorhombic to the rhombohedral phase, respectively. The fraction of the rhombohedral

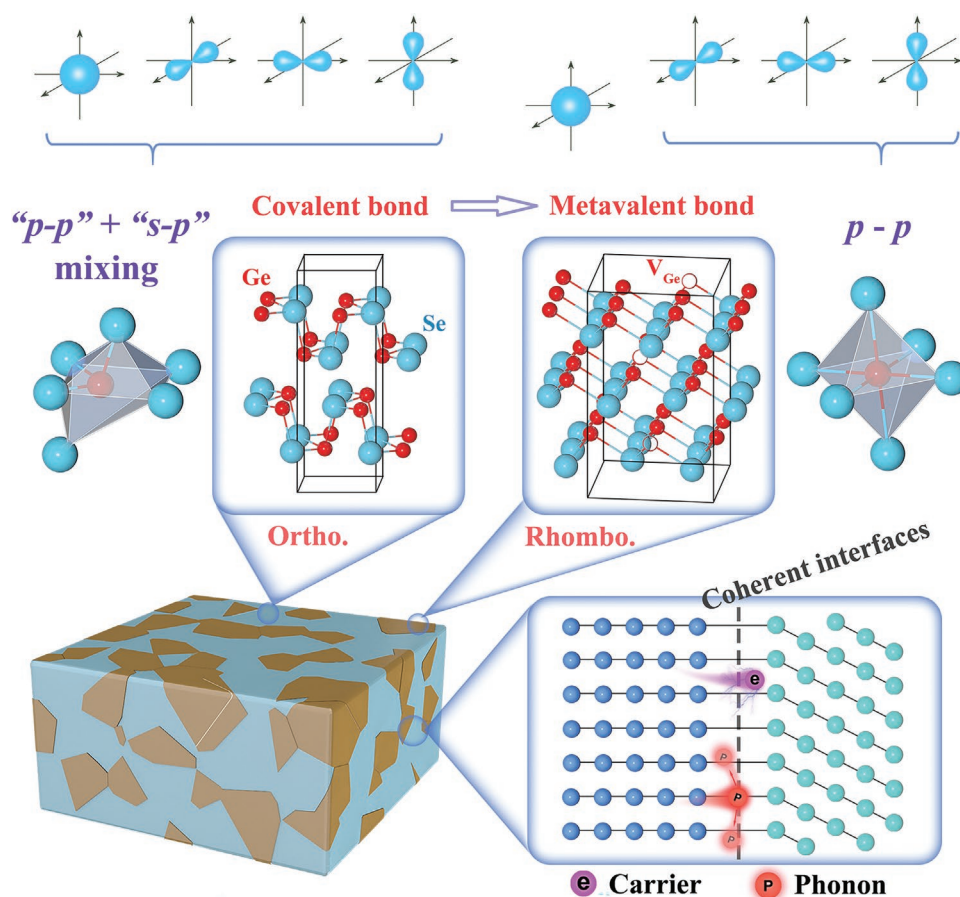


Figure 1. Schematic representation of the formation of the orthorhombic and rhombohedral mixture by tailoring the chemical bonds. The rhombohedral phase contains cation vacancies, increasing the hole carrier concentration and thus the electrical conductivity. It also shows more favorable energy band structures such as a larger valley degeneracy, ensuring a high Seebeck coefficient. The interface between two phases with different chemical bonding mechanisms but close chemical compositions enhance the phonon scattering yet allows electron transmission. All these characteristics are beneficial to improved TE performance.

GeSe phase increases with the content of InTe. The formation of the MVB phase facilitates the fine-tuning of properties upon chemical doping.^[19] In contrast, it is difficult to dope the covalent GeSe phase.^[20] Atom probe tomography (APT) confirms higher contents of dopants (Ag and Cd) and transmission electron microscopy (TEM) shows vacancy layers in the rhombohedral MVB phase. These vacancies and dopants are responsible for the increased charge carrier concentration and significantly improved electrical conductivity. TEM further reveals a coherent interface between the orthorhombic and rhombohedral GeSe phases, beneficial for decent charge carrier mobility. In addition, the acoustic phonon mismatch between the two phases due to distinct chemical bonding mechanisms combined with the induced In-rich nano-clusters and point defects lead to an ultralow thermal conductivity. As a consequence, a maximum zT of ≈ 0.95 at 773 K is achieved in $\text{Ge}_{0.97}\text{Cd}_{0.03}\text{Ag}_{0.03}\text{Se}(\text{InTe})_{0.15}$. This work indicates that in situ design and manipulation of mixed dual phases by tailoring chemical bonds is an effective method for enhancing the TE performance of GeSe and other chalcogenides with different phases.

2. Results and Discussion

Figure 2a displays the X-ray diffraction patterns of $\text{Ge}_{1-y-z}\text{Cd}_y\text{Ag}_z\text{Se}(\text{InTe})_x$. The pristine binary GeSe can be

indexed to the orthorhombic phase (JCPDS#48-1226). Upon InTe alloying, the phase composition transforms from a pure orthorhombic phase to a mixture of orthorhombic and rhombohedral phases. The mixed dual-phase structure remains upon further doping with Cd and Ag. It is worth mentioning that Ge impurities can be observed in all doped samples, which are frequently detected in rhombohedral GeSe.^[21] The resulting Ge vacancies lead to a high carrier concentration.^[22] Furthermore, the production of the rhombohedral phase by InTe alloying promotes the solubility of dopants such as Cd and Ag. Based on the Rietveld refinement (Figure 2b), the normalized ratio of rhombohedral to orthorhombic phase significantly increases with increasing the InTe content, while only slightly increasing with Cd doping. A scanning electron microscope (SEM) was employed to investigate the composite phases as shown in Figures S1–S3 (Supporting Information). Unfortunately, the close contrast makes it difficult to intuitively identify the existence of two phases, but Ge precipitates can be revealed by energy dispersive spectroscopy (EDS). Different from the secondary electron contrast, the two phases show distinguishable optical contrasts under a metallographic microscope. The dual phases with discernible interfaces are apparent in all samples as shown in Figure 2c and Figure S4 (Supporting Information). The ratio of the rhombohedral to orthorhombic phases remarkably increases with the InTe content while only slightly changing

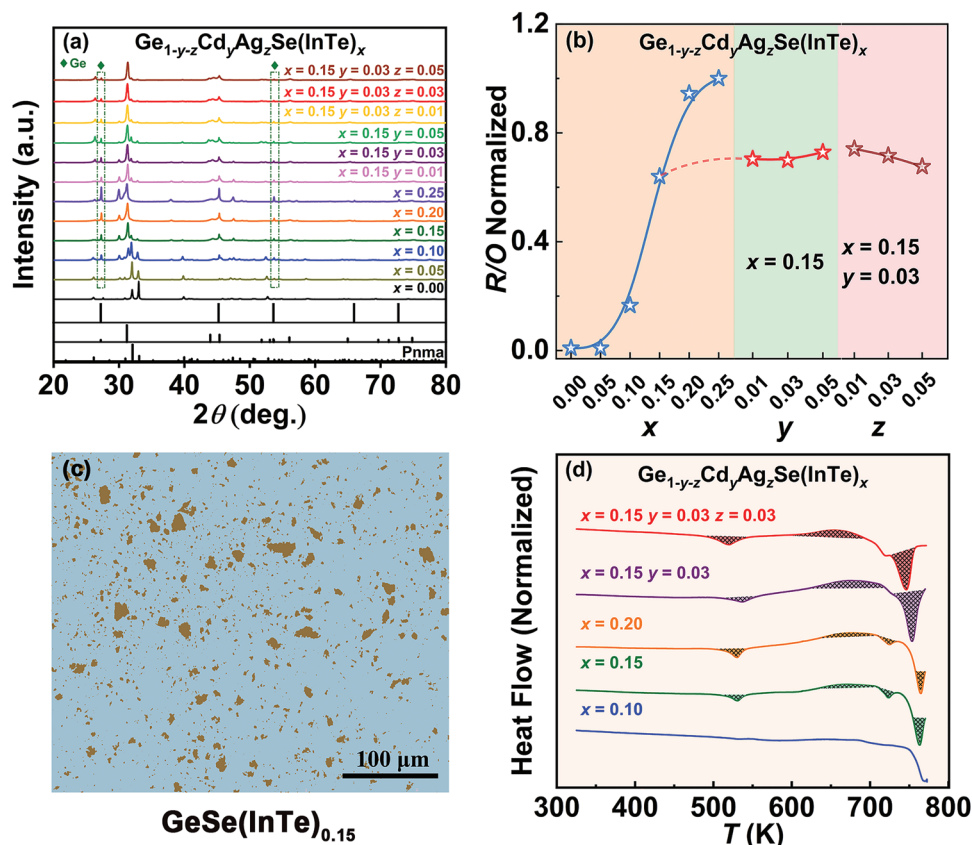


Figure 2. Phase evolution with InTe alloying and Cd-Ag doping in GeSe. a) X-ray diffraction patterns of $\text{Ge}_{1-y-z}\text{Cd}_y\text{Ag}_z\text{Se}(\text{InTe})_x$. b) Rietveld refinement analysis of the normalized ratio of rhombohedral (R) to orthorhombic (O) phase. c) The metallographic microscope analysis of $\text{GeSe}(\text{InTe})_{0.15}$. d) Differential scanning calorimetry (DSC) measurements. The endothermic peak ≈ 730 K of $x = 0.15$ and 0.20 sample corresponds to the formation of the In_4Te_3 phase.

with Cd-Ag doping, consistent with the Rietveld refinement analysis. This demonstrates that InTe is the dominant agent promoting the formation of the rhombohedral phase. Ag mainly tunes the charge carrier concentration and enhances the point defect phonon scattering, as will be discussed below.

Given the complex phase structure resulting from the InTe alloying and Cd-Ag doping, the phase evolution with temperature should also be considered. Here, differential scanning calorimetry (DSC) is carried out to explore the phase structure of $\text{Ge}_{1-y-z}\text{Cd}_y\text{Ag}_z\text{Se}(\text{InTe})_x$ at elevated temperatures. As shown in Figure 2d, the successive endothermic and exothermic peaks of DSC curves with increasing temperature evidence the phase transition, which endows the particularity in the structure of the material. Taking $\text{Ge}_{0.94}\text{Cd}_{0.03}\text{Ag}_{0.03}\text{Se}(\text{InTe})_{0.15}$ as an example, the characteristic peaks at ≈ 530 , ≈ 670 and ≈ 763 K correspond to the phase transition from rhombohedral to cubic (endothermic peak), from metastable rhombohedral to stable hexagonal (exothermic peak), and from hexagonal to cubic (endothermic peak), respectively. These different phases impact the TE performance distinctively as will be discussed in detail later.

To investigate the origin of the phase transition of GeSe upon the addition of InTe, we characterized the elemental distribution in different phases using atom probe tomography (APT). Figure 3a shows the 3D map of $\text{GeSe}(\text{InTe})_{0.15}$ with each atom depicted by a point. The interfaces are highlighted by iso-composition surfaces, for example, the Te-rich interface with a 10 at.% Te concentration in green and the Ge-rich interface with a 60 at.% Ge concentration in red. The corresponding map showing the “probability of multiple events” (PME) is presented in Figure 3b. The PME describes the probability of dislodging more than one ion under a successful laser pulse during the APT measurement.^[23] This value is typically small (below 30%) under a well-controlled condition for most of the materials studied.^[24] Zhu et al. found that the PME value is abnormally large (greater than 60%) for all crystalline *p*-bonded chalcogenides with an octahedral arrangement.^[24] These compounds show a total number of 6 valence electrons (3 per atom) and a coordination number of also 6. Thus, each σ -bond formed by *p*-orbitals is half-filled and differs from the conventional covalent bonding formed by a pair of electrons as described by Lewis.^[17] Moreover, these compounds show a

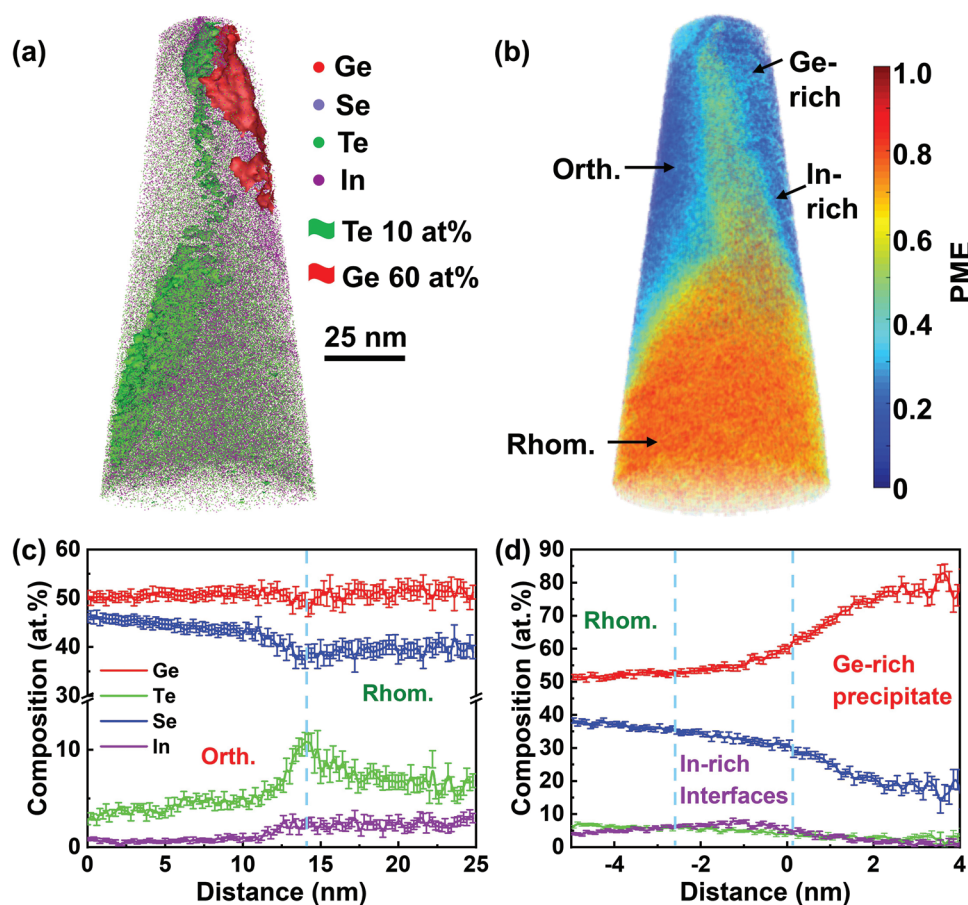


Figure 3. APT results showing the composition and chemical bonding mechanisms of different phases. a) 3D reconstruction of sample $\text{GeSe}(\text{InTe})_{0.15}$ showing the distribution of Ge, Se, In, and Te. b) Corresponding 3D PME map showing different PME values for different phases. c) 1D composition profile measured across the interface from the low-PME part to the high-PME part, showing the correlations between composition and PME. Te enrichment at the interface is observed. d) Composition proximity histogram calculated from the outside (distance < 0) towards the inside (distance > 0) of the Ge-rich isosurface (60 at.% Ge), demonstrating the Ge-rich precipitate and the In-rich interface between the rhombohedral GeSe and the Ge-rich precipitate.

unique combination of properties such as a large optical dielectric constant, a high Born effective charge, and strong lattice anharmonicity.^[15a] All these attributes distinguish this special chemical bonding from covalent, ionic, and metallic bonding, which is thus coined metavalent bonding (MVB). The high PME value is a hallmark of MVB materials.^[24,25] Figure 3c shows the 1D composition profile from the low-PME phase to the high-PME phase across the interface. A small concentration of Te and a negligible concentration of In are found in the low-PME part. In contrast, a much larger concentration of Te and In is found in the high-PME part. Previous work demonstrates that the pure orthorhombic GeSe phase shows a low PME value of $\approx 15\%$.^[24] Thus, we can attribute the low and high PME phases to the orthorhombic and rhombohedral structures, respectively. The more symmetric rhombohedral structure induced by the alloying of InTe can be understood from the orbital energy and thus the chemical bonding mechanisms. As is well known, the covalent bond utilizes electron pairs between nearest neighbors that often includes *s-p* orbital hybridization such as in carbon.^[16b] By contrast, MVB is formed due to the bonding between *p*-orbital electrons where one electron is shared between two adjacent atoms.^[16d] The energy difference between *p*-orbital electrons for Ge and Te is much smaller than that between Ge and Se, which increases the degree of *p*-orbital overlap and weakens *s-p* orbital hybridization. These factors reduce the Peierls distortion and facilitate the formation of MVB. The phase transition from orthorhombic to rhombohedral in GeSe-GeTe alloys has been revealed decades ago.^[26] The corresponding change from covalent to metavalent bonding upon increasing GeTe concentration has only recently been observed.^[16c] We prove that it is due to the modification of orbital overlap and thus the chemical bonding mechanisms, where the orthorhombic phase employs covalent bonding while the rhombohedral phase utilizes metavalent bonding.

We notice that the top-right corner of Figure 3b shows low PME but cannot be attributed to the orthorhombic GeSe phase. This part corresponds to the Ge-rich area in Figure 3a as highlighted by a red isosurface. Figure 3d depicts the composition proximity histogram calculated across the Ge-rich interface from the rhombohedral GeSe to the interior of the Ge-rich precipitate. A maximum composition of ≈ 80 at.% of Ge is obtained. Note that we are not reaching the core of the Ge-rich precipitate due to the small field of view of APT.^[27] EDS measurements have demonstrated that the composition of Ge-rich precipitate is almost pure Ge. It is well recognized that Ge is a typical covalently bonded material. Thus, it shows low PME. Figure 3d also reveals In enrichment at the interface between the rhombohedral GeSe and the Ge-rich precipitate, demonstrating the high affinity of In to structural defects. Figure 4a shows the distribution of In in the rhombohedral phase in sample GeSe(InTe)_{0.15}. Some In-rich features can be observed at grain boundaries as indicated by an arrow. A close investigation of a selected cubic region of interest reveals a very high number density of In-rich nano-clusters, as highlighted by the iso-composition surfaces of 13 at.% In in Figure 4b. The composition of In in 3D space is also illustrated in Figure 4c. These In-rich nano-clusters might be stabilized by the strong interaction between dopants and vacancies^[28] due to a large number of cation vacancies available in the MVB phase.^[29] The release of cation vacancies can depopulate the occupied antibonding states and thus alleviates electronic instability.^[29] The corresponding PME map, as shown in Figure 4d, further corroborates the MVB and rhombohedral phase nature of the volume analyzed by APT. It seems that the alloying component InTe has been mainly consumed by the rhombohedral phase, while the orthorhombic GeSe can only dissolve a small amount of Te and negligible In. This information is important for the further optimization of properties by chemical doping. It implies that the formation of the MVB

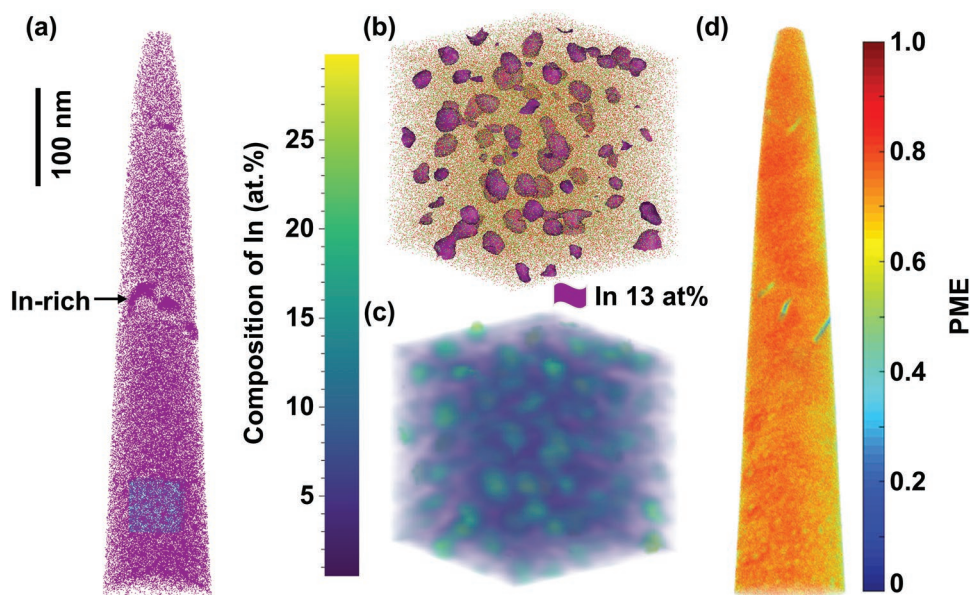


Figure 4. APT results of a single rhombohedral phase in sample GeSe(InTe)_{0.15}. a) Distribution of In in 3D space with obvious In-rich parts indicated by an arrow; other elements are omitted for clarity. b) A close-up of the cubic region of interest selected in Figure 4a showing the In-rich nano-clusters as depicted by the isocomposition surface of 13 at.% In. c) Corresponding volume rendering showing the composition of In in 3D space. d) Corresponding PME map corroborating the MVB feature and rhombohedral phase of the volume probed. Note that the very In-rich parts show low PME.

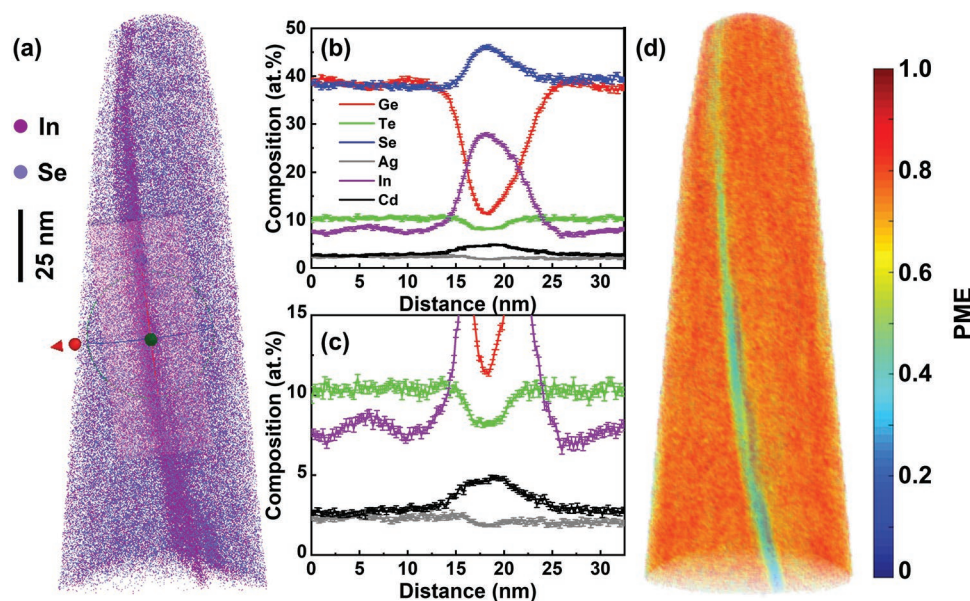


Figure 5. APT results of sample $\text{Ge}_{0.94}\text{Cd}_{0.03}\text{Ag}_{0.03}\text{Se}(\text{InTe})_{0.15}$. a) 3D map showing the distribution of In and Se. Other elements are omitted for clarity. b) Composition profile along the red arrow of the cuboid region of interest in Figure 5a, showing the variation of stoichiometry across the grain boundary. c) A close-up of Figure 5b showing the composition profile of dopants. d) Corresponding PME map, demonstrating the MVB nature of the rhombohedral matrix phase and the collapse of MVB at the grain boundary.

rhombohedral phase increases the dopability of the mixed GeSe phases that enables a fine tuning of the electron and phonon transport by introducing appropriate dopants.

After obtaining the dual-phase GeSe, Cd and Ag were introduced to tune the charge carrier concentration and the lattice thermal conductivity. Figure 5a shows the distribution of In and Se in sample $\text{Ge}_{0.94}\text{Cd}_{0.03}\text{Ag}_{0.03}\text{Se}(\text{InTe})_{0.15}$, other elements are omitted for clarity. A grain boundary enriched in In can be clearly observed. Figure 5b presents the composition profile across this grain boundary within the selected cuboid region of interest. Besides the In-rich character, we also observed the enrichment of Se and the depletion of Ge at the grain boundary. A close-up of the composition profile for low-content dopants demonstrates that the grain boundary is also enriched in Cd and depleted in Te and Ag (Figure 5c). Grain boundaries normally contain more free volume and are of higher energy compared with their adjacent grains. Thus, they are the preferential sites for segregation and precipitation.^[30] The local transport properties will also be influenced by the modification of grain boundary chemistry. The content of Te in the matrix is very close to the value measured in Figure 3c for the rhombohedral phase. This further demonstrates that Te is the key factor that drives the phase transition by tailoring chemical bonds. The compositions of Ag, Cd, and In in the rhombohedral phase are close to or even higher than their nominal values since the orthorhombic phase contains a very limited amount of dopants. These dopants mainly occupy the positions of Ge in the rhombohedral phase. This also explains why the fraction of the rhombohedral phase does not change distinctively with the addition of Cd and Ag, as shown in Figure 2b. We also plot the PME map of the sample characterized, indicating its MVB nature. The In-rich phase at the grain boundary shows a much lower PME value, implying that the bonding mechanism has been changed there.

Figure 6a shows the presence of two different regions characterized by transmission electron microscopy (TEM). Selected area electron diffraction (SAED) was performed to determine their diffraction patterns and thus the crystal structure. The patterns in Figure 6b taken from the upper part of Figure 6a can be indexed to the orthorhombic GeSe phase projected along [001] direction. The high-resolution atomic structures and corresponding models for this orthorhombic phase are also depicted in Figure 6c. The patterns in Figure 6e taken from the middle part of Figure 6a belong to the rhombohedral structure viewed along [-101] direction. The corresponding high-resolution atomic structures of the rhombohedral GeSe are shown in Figure 6f, which fit well the atomic models. This further corroborates the coexistence of dual phases. We also observed a high density of stripe-like defects in the rhombohedral phase (Figure 6d). They can be attributed to the vacancy layers as frequently found in rhombohedral germanium chalcogenide alloys.^[31] Figure 6g shows the interface between these two phases as distinguished by different phase contrasts. A yellow square region including the interface is processed by the inverse fast Fourier transform (IFFT) method to better view the lattice alignment across the interface. Figure 6h demonstrates a coherent interface with no significant elastic strain (Figure 6i) there due to its coherent nature. The formation of coherent interfaces should be related to the in situ phase transition via tailoring chemical bonds. Since both the rhombohedral and orthorhombic phases can be considered special forms of the cubic phase but with different degrees of Peierls distortion,^[18] the interfaces between them could tolerate the lattice mismatch by adjusting the degree of Peierls distortion. The gradual composition transition at the interface as shown in Figure 3b also supports this conjecture. As a result, forming a coherent interface could be more energetically favorable.

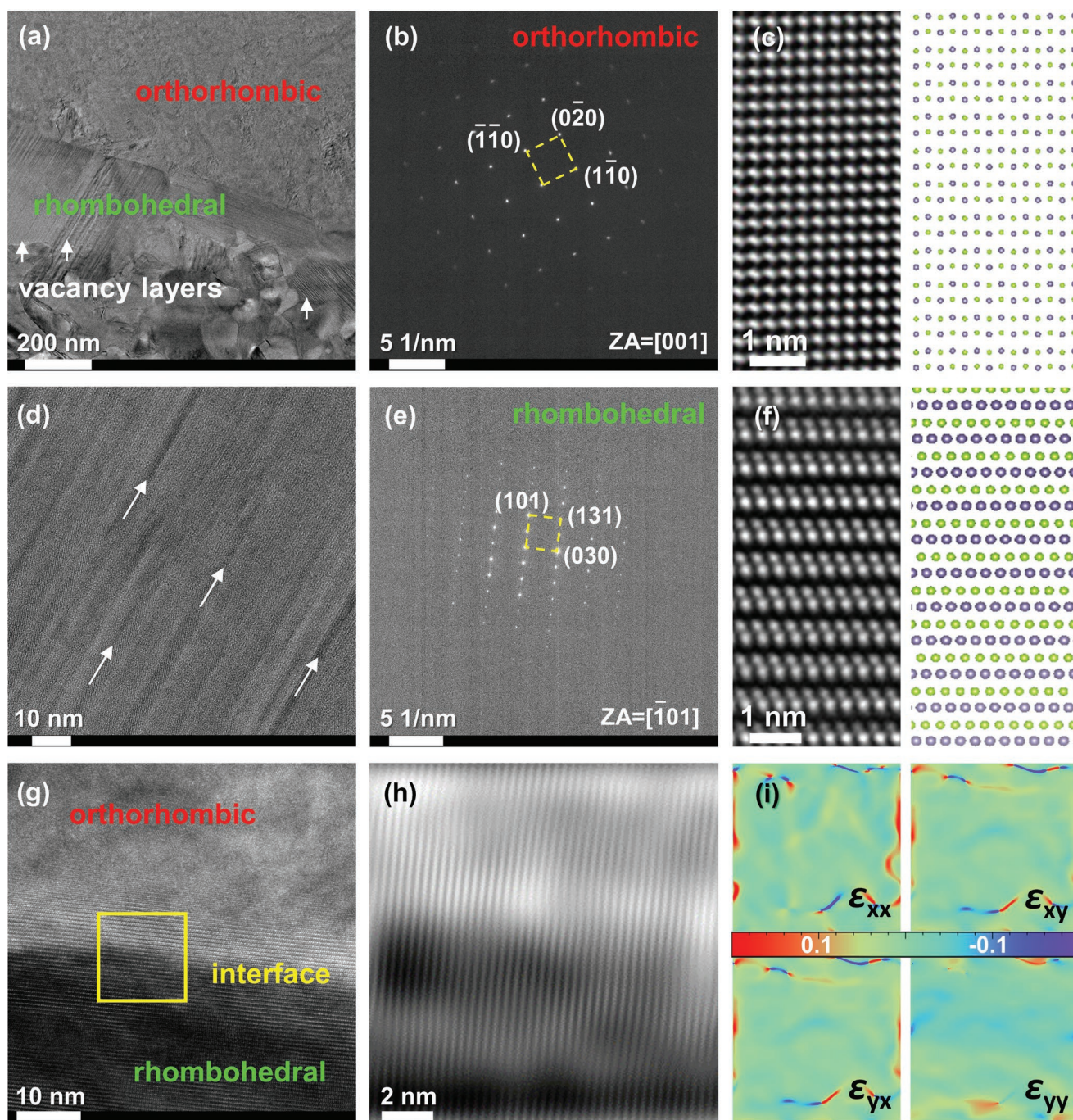


Figure 6. Structural characterization of the dual-phase $\text{GeSe}(\text{InTe})_{0.15}$ by TEM. a) An overview of different grains and phases. b) SAED of the upper part in Figure 6a showing the diffraction pattern of orthorhombic GeSe along $[001]$ direction. c) IFFT image of the orthorhombic phase and corresponding atomic models along $[001]$ direction. d) Vacancy layers inside the grain of the rhombohedral phase as indicated by arrows. e) SAED of the middle part of Figure 6a that can be indexed to the rhombohedral GeSe along $[-101]$ direction. f) IFFT image of the rhombohedral phase and corresponding atomic models along $[-101]$ direction. g) The interface between the orthorhombic and rhombohedral GeSe phases. h) IFFT of the yellow frame indicated in Figure 6g showing the coherent nature of the interface. i) Corresponding strain maps of the interfacial area analyzed by geometric phase analysis (GPA) method.

The TE properties change significantly with increasing the fraction of the rhombohedral phase. **Figure 7a** shows a very low carrier concentration n_{H} of $\approx 1 \times 10^{16} \text{ cm}^{-3}$ for the pristine GeSe due to its high formation energy of Ge vacancies, which is one of the main reasons for the inferior TE performance of

orthorhombic GeSe .^[20,22a] The n_{H} increases continuously with increasing the content of InTe and thus the fraction of the rhombohedral GeSe phase. A large n_{H} value of $\approx 5 \times 10^{19} \text{ cm}^{-3}$ is obtained for the $x = 0.15$ sample. The increase of n_{H} by orders of magnitude is mainly attributed to the formation of

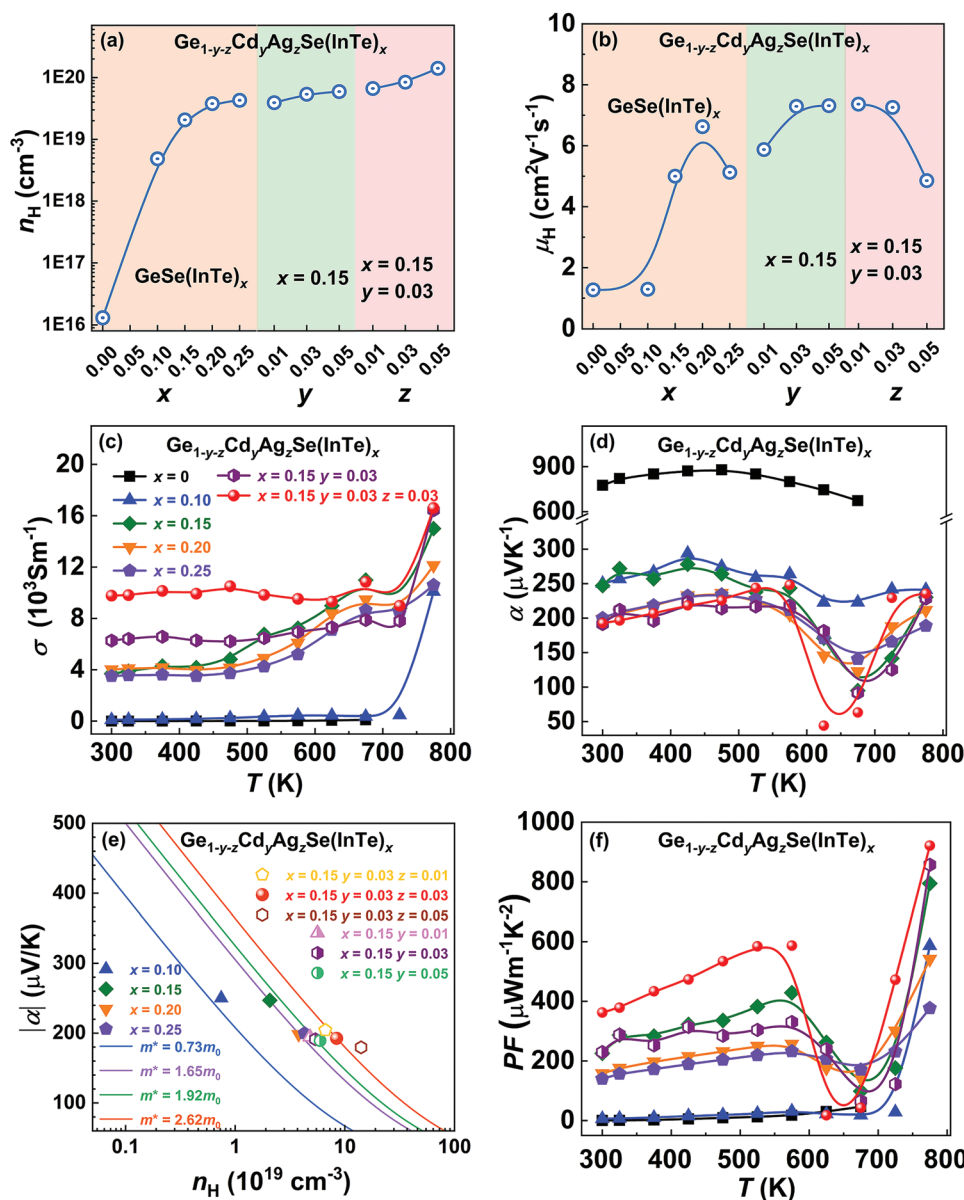


Figure 7. Electrical transport properties of $\text{Ge}_{1-y-z}\text{Cd}_y\text{Ag}_z\text{Se}(\text{InTe})_x$. a) Room-temperature Hall carrier concentration and b) carrier mobility. The temperature dependence of c) electrical conductivity, d) Seebeck coefficient, e) Pisarenko plot calculated based on the single parabolic band (SPB) model. f) Power factor as a function of temperature. The TE performance of sample $x=0.05$ is almost identical to that of the pristine GeSe and thus not presented.

the MVB phase with a high Ge vacancy concentration, which can also be observed from the vacancy layers in Figure 6d. It has been demonstrated that the MVB phase contains a large population of antibonding states.^[15a,29] The formation of cation vacancies is energy favorable to lower the Fermi level and thus to depopulate the occupied antibonding states.^[29] This is the main reason for the much-increased n_H with the introduction of the MVB phase. Many Ge precipitates have also been found within the rhombohedral phase by electron backscattered diffraction (EBSD) and APT, as shown in Figure S5 (Supporting Information). Moreover, doping Cd and Ag further increases n_H to $\approx 1 \times 10^{20}\text{cm}^{-3}$ because Cd can slightly increase the rhombohedral phase content^[21a] and Ag is an effective acceptor in rhombohedral GeSe.^[20] This provides more degrees of freedom

to fine-tune the TE transport properties thanks to the high dopability of the MVB rhombohedral phase. In contrast, the pristine covalent orthorhombic GeSe phase is hardly dopable.^[20]

Besides the optimized n_H , the rhombohedral phase also shows a higher carrier mobility μ_H . MVB materials are also called incipient metals with intrinsically no bandgap given by their half-filled σ -bond.^[16a] Peierls distortion and charge transfer can open the bandgap E_g .^[16c,32] The rhombohedral GeSe has a much smaller degree of Peierls distortion than that of the orthorhombic phase and thus a narrower bandgap.^[33]

According to the description of a Kane band $\frac{\hbar k^2}{2m^*} = E(1 + \frac{E}{E_g})$ (where E is energy, k is the wave vector and \hbar is the reduced Planck's constant), the band effective mass m_b^* will also be

lowered due to the shrinkage of the bandgap.^[34] This is partly responsible for the increased μ_{H} as shown in Figure 7b. In general, however, the TE composites contain more complex interfaces, which are often detrimental to carrier transport. In our case, the dual phases generated by the chemical bond tailoring led to coherent interfaces between the orthorhombic and rhombohedral GeSe (Figure 6, TEM), which will not scatter charge carriers strongly and thus maintain a decent μ_{H} . We noticed that the carrier mobility is lowered in sample $x = 0.25$ although it has a higher content of the rhombohedral phase. This is mainly because the increased content of In in the matrix increases the point defect scattering to charge carriers. In addition, the nominal content of In in sample $x = 0.25$ is higher than the solubility limit measured by APT. This could promote the formation of In-rich precipitates, which further scatter charge carriers and lower carrier mobility. The reduced μ_{H} at a high concentration of Ag dopants is due to the charge carrier scattering by point defects and the increased carrier concentration.^[35]

The formation of orthorhombic and rhombohedral dual-phase GeSe by tailoring the chemical bonds regulates the carrier transport and thus the electrical properties. Figure 7c displays the electrical conductivity σ as a function of temperature. An ultralow room temperature σ of $\approx 0.26 \text{ S m}^{-1}$ is found in pristine orthorhombic GeSe, which gradually increases to $\approx 3700 \text{ S m}^{-1}$ for GeSe(InTe)_{0.15}, an increase by four orders of magnitude. The significant increase in σ is derived from the increasing fraction of the rhombohedral phase, which simultaneously raises n_{H} and μ_{H} . This indicates the effectiveness of introducing the MVB phase in optimizing σ of GeSe. In addition, the σ continuously increases with further Cd and Ag doping (Figure 7c; Figure S6a, Supporting Information), which originates from the slightly increased fraction of rhombohedral phase and the acceptor doping effect of Ag. Notably, a maximum σ of $\approx 16\,600 \text{ S m}^{-1}$ at 773 K is achieved in the Ge_{0.94}Cd_{0.03}Ag_{0.03}Se(InTe)_{0.15} sample.

In thermoelectrics, high electrical conductivity is often averse to a high Seebeck coefficient α given their counter-dependence on n_{H} .^[4a] As shown in Figure 7d, we find that α of InTe alloyed samples is much lower than that of pristine GeSe. For example, the room temperature α decreases from 775 $\mu\text{V K}^{-1}$ for the pristine GeSe to 246 $\mu\text{V K}^{-1}$ for GeSe(InTe)_{0.15}. The dramatically declined α between pristine GeSe and InTe alloyed samples mainly results from the formation of the rhombohedral phase, which significantly increases n_{H} (Figure 7a). In addition, the rhombohedral phase promotes the solubility of Cd and Ag, which further mildly decreases α (Figure 7d; Figure S6b, Supporting Information).

Even though the n_{H} reaches values of the order of 10^{20} cm^{-3} , the α obtained remains at relatively large values. This indicates a modification of the density-of-states (DOS) effective mass m^* because α is closely related to both m^* and n_{H} based on the Pisarenko relationship:^[36] $S = \frac{8\pi^2 k_{\text{B}}^2}{3eh^2} m^* T \left(\frac{\pi}{3n_{\text{H}}} \right)^{2/3}$, where k_{B} is the Boltzmann constant, e is the electron charge, h is Planck's constant. Figure 7e shows the Pisarenko lines calculated based on a single parabolic band (SPB) model.^[37] The m^* increases from 0.73 m_0 for the pristine GeSe to 1.65 m_0 for GeSe(InTe)_{0.15} with the increased fraction of the rhombohedral phase. This

seems contradictory to our arguments that the rhombohedral phase has a lower effective mass leading to high μ_{H} . Note that the μ_{H} is determined by the band effective mass m_{b}^* , which is linked to the DOS m^* by $m^* = (N_{\text{V}})^{2/3} m_{\text{b}}^*$, where N_{V} is the band degeneracy.^[38] The increased m^* and decreased m_{b}^* with increasing the fraction of rhombohedral GeSe demonstrates that the rhombohedral phase must have a larger value of N_{V} . This can be understood from a chemical bonding perspective. As we have proven by APT, the rhombohedral phase utilizes MVB. MVB is formed by the p -band σ -bonds that are orthogonal to each other, giving rise to octahedral coordination.^[14b,16d] In this case, the crystal structure and corresponding Brillouin zone are more symmetric than that of the orthorhombic phase utilizing covalent bonding.^[15] As a result, more equivalent pockets are available for the charge transport and thus a larger N_{V} value is obtained for the rhombohedral phase. The further increase in m^* with Ag doping may be attributed to the increased n_{H} that facilitates the participation of more valence bands with lower energy in the electrical transport. Density functional theory calculations have predicted that the L, Σ , and Z valence bands can all contribute to the charge transport at a high doping level given the small energy differences between them.^[39] The enhanced N_{V} and m^* compensate for the adverse effect of high n_{H} on α , which is critical to obtain a high σ and decent α simultaneously. The dramatical decrease and then increase in α between 600 K and 750 K can be explained by the formation of a hexagonal phase at $\approx 670 \text{ K}$ and its subsequent transformation into a cubic phase at high temperatures, as unraveled by DSC measurements (Figure 2d). The hexagonal GeSe phase shows a very high n_{H} but only an N_{V} value of one, leading to seriously reduced Seebeck coefficients.^[15b,21a] Removing this hexagonal phase via tailoring the chemical bonds by suitable doping or alloying guarantees a further improvement of the average zT value and is an interesting future work.

Benefitting from the simultaneous optimization of n_{H} , μ_{H} , and m^* in the rhombohedral phase caused by chemical bond tailoring, a high-power factor PF is achieved. As shown in Figure 7f, the room temperature PF increases from $\approx 0.22 \mu\text{W m}^{-1} \text{ K}^{-2}$ for pristine GeSe to $\approx 225.7 \mu\text{W m}^{-1} \text{ K}^{-2}$ for GeSe(InTe)_{0.15}, an increase by three orders of magnitude. In addition, the rhombohedral phase improves the solubility limit of Cd and Ag, leading to a further increased PF in Cd- and Ag-doped samples. Notably, a maximum PF of $\approx 921.4 \mu\text{W m}^{-1} \text{ K}^{-2}$ at 773 K is achieved for the Ge_{0.94}Cd_{0.03}Ag_{0.03}Se(InTe)_{0.15} sample.

Other than the optimization of electrical transport performance, the formation of dual-phase mixtures by chemical bond tailoring is also conducive to the optimization of thermal transport properties. The total thermal conductivity κ as a function of temperature is displayed in Figure 8a and Figure S7a (Supporting Information). Obviously, the κ of Ge_{1-y-z}Cd_yAg_zSe(InTe)_x is much lower than that of pristine GeSe around room temperature while slightly rising at elevated temperatures. Specifically, the room temperature κ of pristine GeSe is $\approx 1.77 \text{ W m}^{-1} \text{ K}^{-1}$, while it drops to $\approx 0.95 \text{ W m}^{-1} \text{ K}^{-1}$ for Ge_{0.94}Ag_{0.03}Cd_{0.03}Se(InTe)_{0.15}. The total thermal conductivity κ consists of lattice thermal conductivity κ_{L} and electronic thermal conductivity κ_{e} . The κ_{e} is proportional to σ based on the Wiedemann-Franz law $\kappa_{\text{e}} = L\sigma T$, where L is the Lorenz number estimated by the formula $L = 1.5 + \exp(-|\alpha|/116)$.^[40] Figure 8b shows that κ_{L} of InTe alloyed

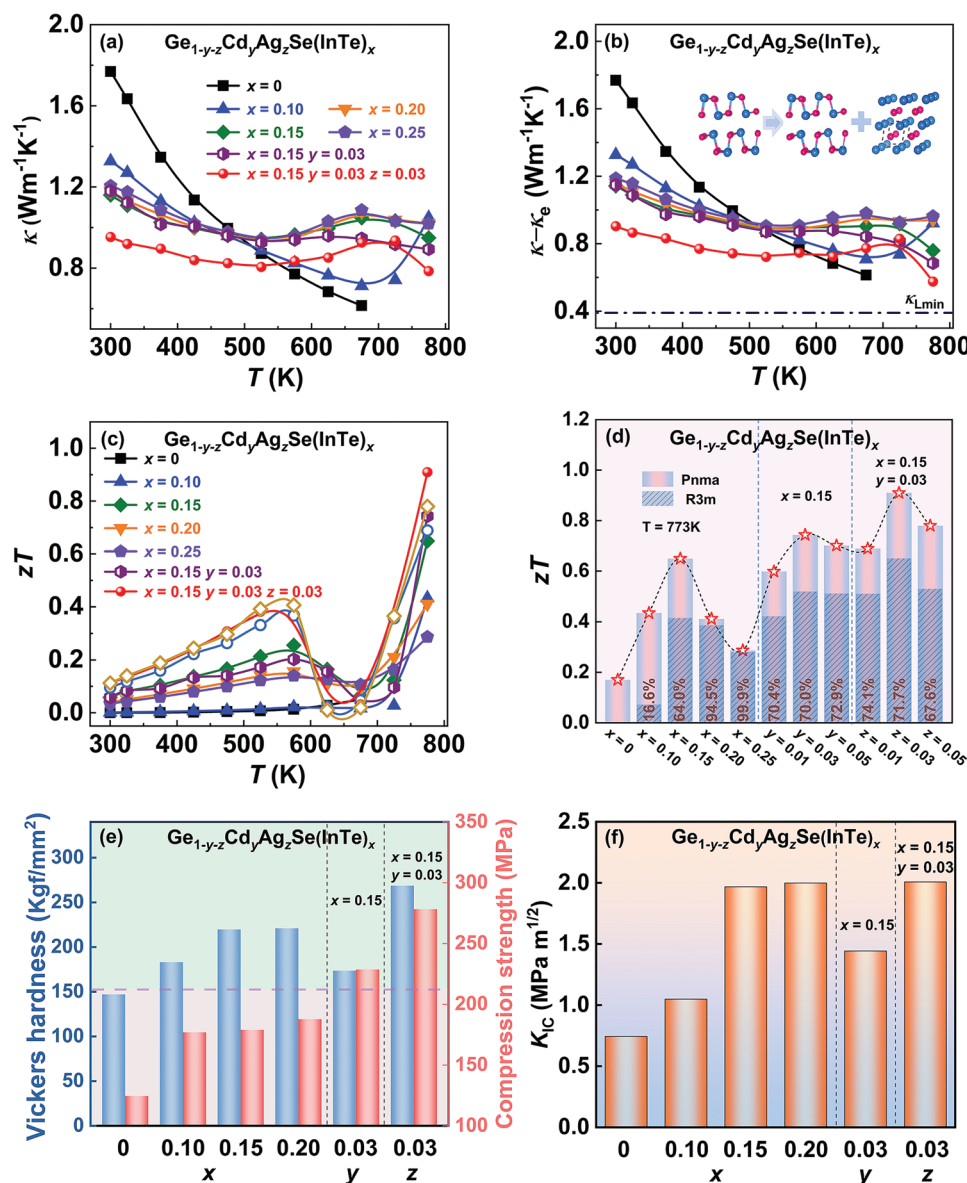


Figure 8. Temperature dependence of a) thermal conductivity, b) lattice thermal conductivity and c) figure of merit zT values of $\text{Ge}_{1-y-z}\text{Cd}_y\text{Ag}_z\text{Se}(\text{InTe})_x$. d) The figure of merit zT values at 773 K with the different ratios of rhombohedral to orthorhombic phase. e) Vickers hardness and compression strength, and f) fracture toughness of $\text{Ge}_{1-y-z}\text{Cd}_y\text{Ag}_z\text{Se}(\text{InTe})_x$.

samples decreases significantly as compared to pristine GeSe around room temperature. The reduced κ_L is derived from the following aspects: i) the rhombohedral phase with MVB has a strong lattice anharmonicity that contributes to the intrinsically low κ_L .^[15a] ii) the phonon mismatch between the dual phases due to the distinct chemical bonding mechanisms enhances the interfacial phonon scattering.^[25,41] iii) the cation vacancies trap the dopants generating In-rich nano-clusters strengthening phonon scattering.^[42] The continuously reduced κ_L with Cd and Ag doping is mainly due to the phonon scattering at point defects benefiting from the increased solubility of dopants in the MVB phase (Figure S7b, Supporting Information).^[43] As for the slightly increased κ_L at elevated temperatures, we speculate that it mainly stems from the complex phase transition

(Figure 2d). Notably, a minimum κ_L of $\approx 0.58 \text{ Wm}^{-1} \text{K}^{-1}$ at 773 K is achieved in $\text{Ge}_{0.94}\text{Ag}_{0.03}\text{Cd}_{0.03}\text{Se}(\text{InTe})_{0.15}$, which is a relatively low value for GeSe-based alloys.

Owing to the optimized electrical and thermal transport properties upon the design of orthorhombic and rhombohedral dual phases as analyzed above, the final thermoelectric figure of merit zT can be significantly improved via tailoring the chemical bonds. As shown in Figure 8c, the maximum zT value of InTe alloyed samples achieves 0.65 at 773 K in $\text{GeSe}(\text{InTe})_{0.15}$, which is ≈ 13 times higher than that of pristine GeSe with the peak zT of 0.05 at 673 K. A further enhanced zT value of ≈ 0.95 at 773 K is obtained in $\text{Ge}_{0.94}\text{Cd}_{0.03}\text{Ag}_{0.03}\text{Se}(\text{InTe})_{0.15}$ (Figure 8c; Figure S8, Supporting Information). Even though this value is lower than the record-high one reported for GeSe-based

alloys,^[21a] it is much larger than the element-doped GeSe^[20] and comparable to state-of-the-art GeSe alloys.^[11a,14c,44] Our work is of more fundamental significance to the design of thermoelectrics by tailoring chemical bonds rather than only pursuing a record-high zT . We also plotted the zT value at 773 K accompanied by the ratio of rhombohedral to orthorhombic phase as a function of composition in Figure 8d. Higher zT values are often achieved at the ratio of rhombohedral to orthorhombic being $\approx 70\%$, indicating the effectiveness of designing the dual-phase structure for TE performance optimization.

Other than the optimization of TE performance, the design of a dual-phase composite is also beneficial to attain the trade-off between strength and ductility,^[2] which is crucial to the long-term service of TE devices.^[4a] As shown in Figure 8e, an ultrahigh Vickers hardness of 269 kgf mm⁻² and compression strength of 278 MPa are achieved in Ge_{0.94}Cd_{0.03}Ag_{0.03}Se (InTe)_{0.15} because of the dual-phase strengthening and solid solution strengthening that impede the dislocation movement.^[45] Unexpectedly, this sample also exhibits a good fracture toughness (K_{IC}) of 2 Mpa m^{-1/2} owing to dual-phase toughening that restrains the propagation of micro-cracks (Figure 8f).^[46] Our results open the avenue for designing dual-phase TE composites with advanced strength-ductility combinations.

3. Conclusions

In this work, the orthorhombic and rhombohedral dual phases with the same major constituting elements are generated in situ by alloying GeSe with InTe via chemical bond tailoring. Atom probe tomography shows evidence for the formation of a rhombohedral phase utilizing metavalent bonding, which is mainly attributed to the dopant of Te. Benefitting from the increased fraction of rhombohedral MVB phase, the charge carrier concentration and carrier mobility, the band degeneracy, and the density-of-states effective mass are all improved, leading to a considerable increase in the power factor. Furthermore, the MVB phase shows a strong lattice anharmonicity and thus intrinsically low lattice thermal conductivity. In addition, the different chemical bonding mechanisms between the orthorhombic and rhombohedral GeSe phases generate a large acoustic phonon mismatch and enhance the phonon scattering at interfaces. The cation vacancies in the MVB phase interact with dopants forming nano-clusters, which can also scatter phonons at a certain frequency range. These factors result in an ultralow lattice thermal conductivity and enhanced TE performance. The rhombohedral phase also provides extra freedom for chemical doping (Cd and Ag) to further optimize the thermoelectric performance. As a consequence, a maximum zT value of 0.95 at 773 K is achieved in Ge_{0.94}Cd_{0.03}Ag_{0.03}Se(InTe)_{0.15}. This work attests to the efficiency of in situ designing dual-phase mixtures by tailoring chemical bonds in enhancing the TE and mechanical performance of GeSe and other related chalcogenides. Moreover, this work also provides a design recipe to form dual-phase thermoelectric chalcogenides by referring to the “treasure map” separating different chemical bonding mechanisms as developed by Raty and Wuttig et al.^[16b] The metavalently bonded compounds illustrated on this map with proper compositions can be employed to induce the phase transition.

Supporting Information

Supporting Information is available from the Wiley Online Library or from the author.

Acknowledgements

The work was supported by the National Natural Science Foundation of China (52071218), the China Postdoctoral Science Foundation (2022M722170), the Shenzhen Science and Technology Innovation Commission (20200731215211001, 20200814110413001) and the Guangdong Basic and Applied Basic Research Foundation (2022A1515012492). Y.Y. and M.W. acknowledge support from the German Research Foundation DFG within project SFB917. Y.Y. acknowledges the financial support under the Excellence Strategy of the Federal Government and the Länder within the ERS RWTH Start-Up grant (Grant No. StUpPD_392-21). The authors also appreciate Dr. Quanxin Yang for the Rietveld refinement of XRD data.

Open access funding enabled and organized by Projekt DEAL.

Conflict of Interest

The authors declare no conflict of interest.

Data Availability Statement

The data that support the findings of this study are available from the corresponding author upon reasonable request.

Keywords

chemical bond tailoring, composite engineering, GeSe, metavalent bonding, thermoelectrics

Received: December 20, 2022

Revised: January 16, 2023

Published online: January 31, 2023

- [1] a) S. Duan, N. Man, J. Xu, Q. Wu, G.-q. Liu, X. Tan, H. Shao, K. Guo, X. Yang, J. Jiang, *J. Mater. Chem. A* **2019**, 7, 9241; b) J. Xiao, X. Qi, X. Gong, Q. Peng, Y. Chen, R. Xie, W. Zhong, *J. Mater. Sci. Technol.* **2023**, 139, 137; c) S. Zheng, X. Li, J. Zhang, J. Wang, C. Zhao, X. Hu, Y. Wu, Y. He, *J. Environ. Sci.* **2023**, 125, 1.
- [2] Z. Li, K. G. Pradeep, Y. Deng, D. Raabe, C. C. Tasan, *Nature* **2016**, 534, 227.
- [3] a) J. He, T. M. Tritt, *Science* **2017**, 357, eaak9997; b) T. Zhu, Y. Liu, C. Fu, J. P. Heremans, J. G. Snyder, X. Zhao, *Adv. Mater.* **2017**, 29, 1605884; c) Y. Yu, X. Xu, Y. Wang, B. Jia, S. Huang, X. Qiang, B. Zhu, P. Lin, B. Jiang, S. Liu, X. Qi, K. Pan, D. Wu, H. Lu, M. Bosman, S. J. Pennycook, L. Xie, J. He, *Nat. Commun.* **2022**, 13, 5612.
- [4] a) X.-L. Shi, J. Zou, Z.-G. Chen, *Chem. Rev.* **2020**, 120, 7399; b) P.-C. Wei, C.-N. Liao, H.-J. Wu, D. Yang, J. He, G. V. Biesold-McGee, S. Liang, W.-T. Yen, X. Tang, J.-W. Yeh, Z. Lin, J.-H. He, *Adv. Mater.* **2020**, 32, 1906457; c) X. Xu, Y. Huang, X. Liu, B. Jia, J. Cui, R. He, J. Wang, Y. Luo, K. Nielsch, J. He, *Energy Environ. Sci.* **2022**, 15, 4058.
- [5] D. J. Bergman, O. Levy, *J. Appl. Phys.* **1991**, 70, 6821.
- [6] A. Mehdizadeh Dehkordi, M. Zebajadi, J. He, T. M. Tritt, *Mater. Sci. Eng. R* **2015**, 97, 1.

- [7] D. L. Medlin, G. J. Snyder, *Curr. Opin. Colloid Interface Sci.* **2009**, *14*, 226.
- [8] a) R. Deng, X. Su, S. Hao, Z. Zheng, M. Zhang, H. Xie, W. Liu, Y. Yan, C. Wolverton, C. Uher, M. G. Kanatzidis, X. Tang, *Energy Environ. Sci.* **2018**, *11*, 1520; b) D. Yang, X. Su, J. Li, H. Bai, S. Wang, Z. Li, H. Tang, K. Tang, T. Luo, Y. Yan, J. Wu, J. Yang, Q. Zhang, C. Uher, M. G. Kanatzidis, X. Tang, *Adv. Mater.* **2020**, *32*, 2003730.
- [9] C. Hu, K. Xia, C. Fu, X. Zhao, T. Zhu, *Energy Environ. Sci.* **2022**, *15*, 1406.
- [10] a) J. Li, Q. Tan, J.-F. Li, D.-W. Liu, F. Li, Z.-Y. Li, M. Zou, K. Wang, *Adv. Funct. Mater.* **2013**, *23*, 4317; b) L. Zhao, L. Yu, J. Yang, M. Wang, H. Shao, J. Wang, Z. Shi, N. Wan, S. Hussain, G. Qiao, J. Xu, *Mater. Chem. Phys.* **2022**, *292*, 126669; c) J. Wang, J.-B. Li, H.-Y. Yu, J. Li, H. Yang, X. Yaer, X.-H. Wang, H.-M. Liu, *ACS Appl. Mater. Interfaces* **2020**, *12*, 2687.
- [11] a) Z. Huang, S. A. Miller, B. Ge, M. Yan, S. Anand, T. Wu, P. Nan, Y. Zhu, W. Zhuang, G. J. Snyder, P. Jiang, X. Bao, *Angew. Chem., Int. Ed.* **2017**, *56*, 14113; b) L.-D. Zhao, S.-H. Lo, Y. Zhang, H. Sun, G. Tan, C. Uher, C. Wolverton, V. P. Dravid, M. G. Kanatzidis, *Nature* **2014**, *508*, 373; c) B. Jiang, W. Wang, S. Liu, Y. Wang, C. Wang, Y. Chen, L. Xie, M. Huang, J. He, *Science* **2022**, *377*, 208.
- [12] a) M. Sist, C. Gatti, P. Nørby, S. Cenedese, H. Kasai, K. Kato, B. B. Iversen, *Chem. – Eur. J.* **2017**, *23*, 6888; b) V. L. Deringer, R. P. Stoffel, R. Dronskowski, *Phys. Rev. B* **2014**, *89*, 094303; c) M. Li, S.-D. Xu, M. Hong, W.-Y. Lyu, Y. Wang, M. Dargusch, J. Zou, H.-M. Cheng, Z.-G. Chen, *Adv. Funct. Mater.* **2022**, *32*, 2208579.
- [13] a) H. Yu, D. Gao, X. Wang, X. Du, X. Lin, W. Guo, R. Zou, C. Jin, K. Li, Y. Chen, *NPG Asia Mater.* **2018**, *10*, 882; b) F. O. von Rohr, H. Ji, F. A. Cevallos, T. Gao, N. P. Ong, R. J. Cava, *J. Am. Chem. Soc.* **2017**, *139*, 2771.
- [14] a) C.-F. Schön, S. van Bergerem, C. Mattes, A. Yadav, M. Grohe, L. Kobbelt, M. Wuttig, *Sci. Adv.* **2022**, *8*, eade0828; b) R. Arora, U. V. Waghmare, C. N. R. Rao, *Adv. Mater. n/a*, 2208724; c) D. Sarkar, S. Roychowdhury, R. Arora, T. Ghosh, A. Vasdev, B. Joseph, G. Sheet, U. V. Waghmare, K. Biswas, *Angew. Chem., Int. Ed.* **2021**, *60*, 10350.
- [15] a) Y. Yu, M. Cagnoni, O. Cojocar-Mirédin, M. Wuttig, *Adv. Funct. Mater.* **2020**, *30*, 1904862; b) M. Cagnoni, D. Führen, M. Wuttig, *Adv. Mater.* **2018**, *30*, 1801787.
- [16] a) M. Wuttig, V. L. Deringer, X. Gonze, C. Bichara, J.-Y. Raty, *Adv. Mater.* **2018**, *30*, 1803777; b) J.-Y. Raty, M. Schumacher, P. Golub, V. L. Deringer, C. Gatti, M. Wuttig, *Adv. Mater.* **2019**, *31*, 1806280; c) L. Guarneri, S. Jakobs, A. von Hoegen, S. Maier, M. Xu, M. Zhu, S. Wahl, C. Teichrib, Y. Zhou, O. Cojocar-Mirédin, M. Raghuvanshi, C.-F. Schön, M. Drögel, C. Stampfer, R. P. S. M. Lobo, A. Piarristeguy, A. Pradel, J.-Y. Raty, M. Wuttig, *Adv. Mater.* **2021**, *33*, 2102356; d) M. Wuttig, C.-F. Schön, J. Lötfering, P. Golub, C. Gatti, J.-Y. Raty, *Adv. Mater.* **2022**, *n/a*, 2208485.
- [17] G. N. Lewis, *J. Am. Chem. Soc.* **1916**, *38*, 762.
- [18] J.-Y. Raty, M. Wuttig, *J. Phys. D: Appl. Phys.* **2020**, *53*, 234002.
- [19] Y. Liu, X. Zhang, P. Nan, B. Zou, Q. Zhang, Y. Hou, S. Li, Y. Gong, Q. Liu, B. Ge, O. Cojocar-Mirédin, Y. Yu, Y. Zhang, G. Chen, M. Wuttig, G. Tang, *Adv. Funct. Mater.* **2022**, *32*, 2209980.
- [20] X. Zhang, J. Shen, S. Lin, J. Li, Z. Chen, W. Li, Y. Pei, *J. Materiomics* **2016**, *2*, 331.
- [21] a) Z. Wang, H. Wu, B. Zhang, L. Dai, Y. Huo, Y. Huang, G. Han, X. Lu, X. Zhou, G. Wang, *Adv. Funct. Mater.* **2022**, *32*, 2111238; b) Z. Wang, H. Wu, M. Xi, H. Zhu, L. Dai, Q. Xiong, G. Wang, G. Han, X. Lu, X. Zhou, G. Wang, *ACS Appl. Mater. Interfaces* **2020**, *12*, 41381.
- [22] a) T. Lyu, X. Li, Q. Yang, J. Cheng, Y. Zhang, C. Zhang, F. Liu, J. Li, W. Ao, H. Xie, L. Hu, *Chem. Eng. J.* **2022**, *442*, 136332; b) X. Li, Z. Liang, J. Li, F. Cheng, J. He, C. Zhang, J. Li, F. Liu, T. Lyu, B. Ge, L. Hu, *Nano Energy* **2022**, *100*, 107434; c) B. Duan, Y. Zhang, Q. Yang, Y. Li, J. Cheng, C. Zhang, J. Li, F. Liu, L. Hu, *Adv. Energy Sustainability Res.* **2022**, *3*, 2200124.
- [23] Z. Peng, F. Vurpillot, P.-P. Choi, Y. Li, D. Raabe, B. Gault, *Ultramicroscopy* **2018**, *189*, 54.
- [24] M. Zhu, O. Cojocar-Mirédin, A. M. Mio, J. Keutgen, M. Küpers, Y. Yu, J.-Y. Cho, R. Dronskowski, M. Wuttig, *Adv. Mater.* **2018**, *30*, 1706735.
- [25] D. An, J. Wang, J. Zhang, X. Zhai, Z. Kang, W. Fan, J. Yan, Y. Liu, L. Lu, C.-L. Jia, M. Wuttig, O. Cojocar-Mirédin, S. Chen, W. Wang, G. J. Snyder, Y. Yu, *Energy Environ. Sci.* **2021**, *14*, 5469.
- [26] H. Wiedemeier, P. Siemers, *High Temp. Sci.* **1984**, *17*, 395.
- [27] B. Gault, A. Chiaramonti, O. Cojocar-Mirédin, P. Stender, R. Dubosq, C. Freysoldt, S. K. Makineni, T. Li, M. Moody, J. M. Cairney, *Nat. Rev. Methods Primers* **2021**, *1*, 51.
- [28] H. S. Zurob, H. Seyedrezai, *Scripta Mater.* **2009**, *61*, 141.
- [29] M. Wuttig, D. Lüsebrink, D. Wamwangi, W. Welnic, M. Gilleßen, R. Dronskowski, *Nat. Mater.* **2007**, *6*, 122.
- [30] C. Zhang, G. Yan, Y. Wang, X. Wu, L. Hu, F. Liu, W. Ao, O. Cojocar-Mirédin, M. Wuttig, G. J. Snyder, Y. Yu, *Adv. Energy Mater. n/a*, 2203361.
- [31] a) M. Hong, Y. Wang, W. Liu, S. Matsumura, H. Wang, J. Zou, Z.-G. Chen, *Adv. Energy Mater.* **2018**, *8*, 1801837; b) D. Wu, D. Feng, X. Xu, M. He, J. Xu, J. He, *J. Alloys Compd.* **2019**, *805*, 831.
- [32] S. Maier, S. Steinberg, Y. Cheng, C.-F. Schön, M. Schumacher, R. Mazzarello, P. Golub, R. Nelson, O. Cojocar-Mirédin, J.-Y. Raty, M. Wuttig, *Adv. Mater.* **2020**, *32*, 2005533.
- [33] B. J. Kooi, M. Wuttig, *Adv. Mater.* **2020**, *32*, 1908302.
- [34] a) E. O. Kane, *J. Phys. Chem. Solids* **1957**, *1*, 249; b) Y. Pei, A. D. LaLonde, H. Wang, G. J. Snyder, *Energy Environ. Sci.* **2012**, *5*, 7963.
- [35] F. Zhang, X. Zhao, R. Li, S. He, X. Tan, J. Zhu, R. Ang, *J. Mater. Chem. A* **2022**, *10*, 23521.
- [36] a) R. Moshwan, L. Yang, J. Zou, Z.-G. Chen, *Adv. Funct. Mater.* **2017**, *27*, 1703278; b) M. Cutler, J. F. Leavy, R. L. Fitzpatrick, *Phys. Rev.* **1964**, *133*, A1143.
- [37] A. F. May, E. S. Toberer, A. Saramat, G. J. Snyder, *Phys. Rev. B* **2009**, *80*, 125205.
- [38] Y. Pei, X. Shi, A. LaLonde, H. Wang, L. Chen, G. J. Snyder, *Nature* **2011**, *473*, 66.
- [39] K. Yuan, Z. Sun, X. Zhang, X. Gong, D. Tang, *Phys. Chem. Chem. Phys.* **2020**, *22*, 1911.
- [40] H.-S. Kim, Z. M. Gibbs, Y. Tang, H. Wang, G. J. Snyder, *APL Mater.* **2015**, *3*, 041506.
- [41] C. Rodenkirchen, M. Cagnoni, S. Jakobs, Y. Cheng, J. Keutgen, Y. Yu, M. Wuttig, O. Cojocar-Mirédin, *Adv. Funct. Mater.* **2020**, *30*, 1910039.
- [42] Y. Zhu, D. Wang, T. Hong, L. Hu, T. Ina, S. Zhan, B. Qin, H. Shi, L. Su, X. Gao, L.-D. Zhao, *Nat. Commun.* **2022**, *13*, 4179.
- [43] L. Fu, M. Yin, D. Wu, W. Li, D. Feng, L. Huang, J. He, *Energy Environ. Sci.* **2017**, *10*, 2030.
- [44] a) M. Yan, H. Geng, P. Jiang, X. Bao, *J. Energy Chem.* **2020**, *45*, 83; b) M. Yan, X. Tan, Z. Huang, G. Liu, P. Jiang, X. Bao, *J. Mater. Chem. A* **2018**, *6*, 8215; c) D. Sarkar, T. Ghosh, S. Roychowdhury, R. Arora, S. Sajjan, G. Sheet, U. V. Waghmare, K. Biswas, *J. Am. Chem. Soc.* **2020**, *142*, 12237.
- [45] a) F. Guo, J. Zhu, B. Cui, Y. Sun, X. Zhang, W. Cai, J. Sui, *Acta Mater.* **2022**, *231*, 117922; b) A. Suwardi, S. H. Lim, Y. Zheng, X. Wang, S. W. Chien, X. Y. Tan, Q. Zhu, L. M. N. Wong, J. Cao, W. Wang, Q. Yan, C. K. I. Tan, J. Xu, *J. Mater. Chem. C* **2020**, *8*, 16940.
- [46] C. Ma, X. Bai, Q. Ren, H. Liu, Y. Gu, H. Cui, *J. Mater. Sci. Technol.* **2020**, *58*, 10.